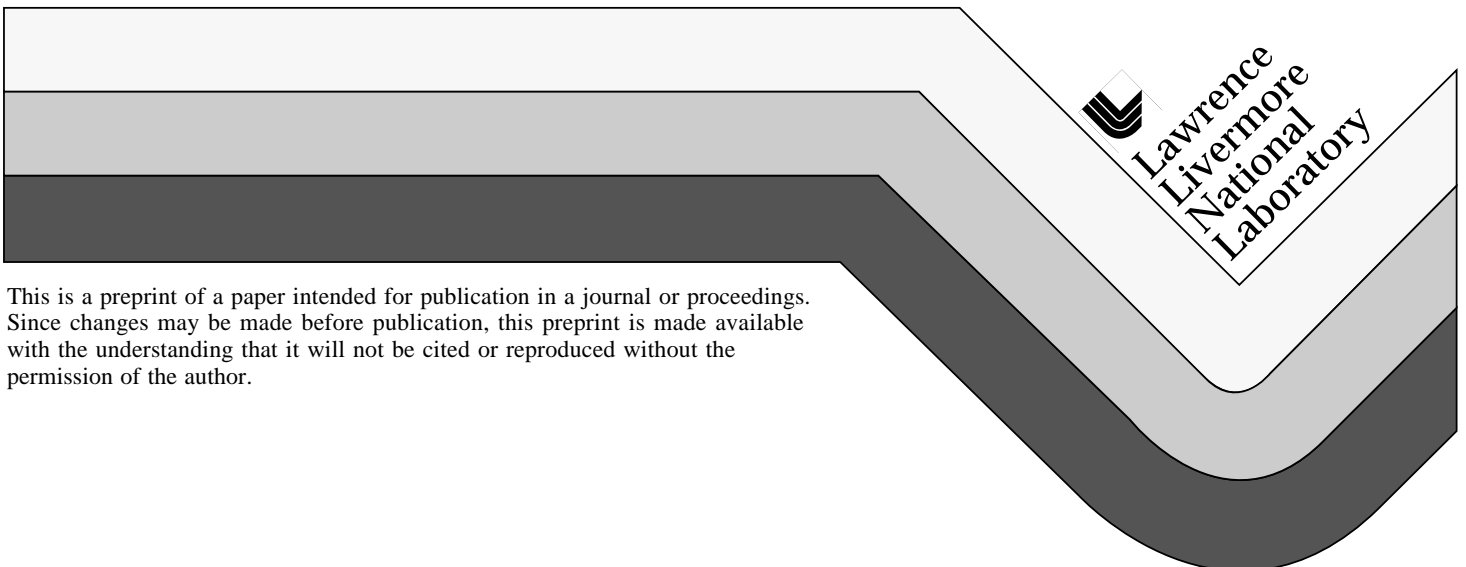# Detection of Leaks in Underground Storage Tanks Using Electrical Resistance Methods

A. Ramirez
W. Daily
A. Binley
D. LaBrecque
D. Roelant

This paper was prepared for submittal to
The Journal of Engineering and Environmental Geophysics

October 1995

Lawrence Livermore National Laboratory

Detection of Leaks in
Underground Storage Tanks
Using Electrical Resistance Methods

Abelardo Ramirez*
William Daily*
Andrew Binley**
Douglas LaBrecque***
David Roelant****

***Lawrence Livermore National Laboratory**
P.O Box 808, L-206
Livermore, CA 94550
off. 510-422-6909
fax 510-422-3118

**** Lancaster University**
***** University of Arizona**
****** BDM Federal, Inc.**

Abstract:

Two field experiments were performed to evaluate the performance of electrical resistance tomography (ERT) as a leak detection method under metal underground storage tanks (UST). This document provides a summary of field experiment results performed under a 15 m diameter steel tank mockup located at the Hanford Reservation, Washington, and of supporting numerical simulations. Two different leak events were created. About 3800 liters of saline solution were first released along a portion of the tank's edge and another 1900 liters were later released near the tank's center. The release rate averaged about 26 liters/hour for the leak on the tank's side and about 3.0 liters/hour for the center leak. Two and three dimensional tomographs were calculated using data collected before, during and after each spill. The tomographs mapped the spatial and temporal evolution of resistivity changes caused by the leak; as the solution penetrated the soil, readily detectable resistivity decreases were observed and used to map the associated plume. The results show that the metal tank has significant effects on the results obtained, primarily in reducing sensitivity to the leak. The field results indicate that the plume associated with these releases could be reliably detected after approximately 190 liters were released. Results are also shown where the metal tank and metal-cased boreholes are used as large electrodes. We use the field results to extrapolate how these techniques could be used to detect and locate leaks, and to delineate any resulting plumes from the underground storage tanks.

1.0 Introduction:

1.1 Leak detection under storage tanks:
Large volumes of hazardous liquids are stored worldwide in surface and underground tanks. Frequently these tanks are found to leak thereby resulting in not only a loss of stored inventory but, more importantly, contamination to soil and groundwater. The Department of Energy (DOE) and its predecessor agencies have accumulated large volumes of hazardous, radioactive and mixed wastes during the research, development and production of nuclear weapons over the past fifty years. The Office of Environmental Management (DOE/EM) has identified the stabilization and remediation of high-level radioactive waste in storage tanks as one of the five major problem areas in the environmental cleanup of its sites and facilities.

The DOE has 332 underground storage tanks at its Hanford, Idaho, Oak Ridge, Fernald, West Valley and Savannah River sites; these store 380,000 cubic meters of high-level waste (HLW) in both liquid and solid forms. The different forms of the waste in the tanks will require a variety of technologies for waste removal and treatment. The wastes are stored in carbon steel, stainless steel or gunnite tanks. The radiolysis of the organic constituents has led to the generation of flammable gases and explosive conditions.

Single shell and the double shell waste tank designs are common throughout the United States. The Department of Defense and industrial activities use thousands of storage tanks primarily for fuels, solvents, and other chemicals. The double shell tank design provides redundant containment barriers and allows detection of leakage prior to escape to the soil. The single shell tanks present potential environmental hazards because only a single barrier contains the liquids and any breach in the barrier will cause contaminant spillage. One method being considered to retrieve the waste is sluicing. This method will require recirculating thousands of gallons of water in the tank. If the sluicing method is used, it is possible to leak HLW into the soil. In other tanks, water is added to keep waste matrix from drying out and providing possible ignition to the flammable gases.

There are two methods of detecting leakage from tanks: monitoring the liquid level of waste in the tanks and monitoring the soil under the tanks for leaks. Liquid level sensors can signal a leak but are limited in sensitivity and provide no information about the location or the leak or the distribution of the resulting plume. For example, Cruse et al., (1995), report that liquid level sensors used at the Dept. of Energy's Hanford Site (Richland, Washington) may detect a change of +/- 2.54 cm. In large diameter tanks (23 m.) such as those present at Hanford, this provides a level sensitivity of +/- 10,200 liters(2700 gallons). Outside the tanks detection is more challenging. It is very expensive to emplace chemical sensors under the tanks and the heterogeneous finger-like structure of liquid transport through soils requires that hundreds of sensors be placed around and underneath a tank to ensure reliable detection of chemical contaminants spills.

The proposed method of subsurface electrical resistance tomography reduces these shortcomings. The strategy of our approach (shown in Fig. 1) is to map the resistivity around and below a tank over time. When the spillage of the liquids changes the electrical resistivity in a measurable way, electrical resistivity tomographs can be used to map the resistivity changes caused by spillage. The pixel elements shown in difference resistivity tomographs behave, in some ways, like an array of point sensors deployed below a tank to detect spillage.

This work was designed specifically to address the issues of leaks from the single shell tanks built by the DOE during the cold war for storage of highly radioactive mixed wastes. The contents of these tanks is highly variable but typically the liquids are highly saline and therefore electrically conductive. For this reason a salt water tracer was used in this field demonstration. For testing, an electrical equivalent (saline solution) was used instead of the real contaminant (radioactive nitrate solutions, see Cruse et al., for details) to preserve the environmental quality of the test site. To test the proposed approach in a field demonstration, we would like to produce a tomograph of the soil under a tank and then, while observing changes of subsurface electrical properties, release the contaminant near the tank to simulate a leak. The results of two field experiments and numerical simulations which followed this approach are described herein. The resulting tomographs are used to evaluate the performance of electrical resistance tomography (ERT) for detecting and locating leaks as well as delineating any resulting plumes emanating from steel storage tanks.

The presence of a metal tank with a resistivity of approximately 10^{-8} ohm-m embedded in soil with a resistivity of 10^2 to 10^3 ohm-m results in resistivity contrasts that are much larger than those found in natural geologic settings. One consequence of this large contrast is that a large fraction of the electrical current transmitted during a survey is shunted through the metal. This causes a significant reduction in the sensitivity of the measurements to the soil properties. Also, many of the assumptions made in formulating the forward and inverse problems are only valid for smaller contrasts. An objective of this work was to evaluate the effects that such a large resistivity contrast will have on the performance of the methods used.

1.1.1 Small-scale proof of concept tests:
Two controlled experiments were conducted at the Oregon Graduate Institute (OGI) to determine if ERT could be used to detect and locate a leak beneath a steel storage tank (refer to Daily et al., (1995) for further details). A 1.8 m diameter metal screen was placed in intimate contact with the soil. This metallic screen served as a scaled down model for the electrical properties of a tank bottom resting directly on the soil. The strategy was to reconstruct an image of the electrical resistivity distribution under this small scale metallic barrier before and during a controlled release of water. Any fluid entering the ground that would change its electrical conductivity might be detected by comparison of the two images.

Comparison of images taken before and during separate releases of brine and tap water clearly showed the changes induced by both fluids. Each simulated leak and its location were imaged as a conductive anomaly centered near the point of origin. The anomalies were also observed to spread with time during each release. These results suggested that the detection and location of leaks from large metal tanks may be possible. The tests described below build on this early work by showing that similar results are observed at a more realistic scale.

1.2 Description of ERT:
Electrical resistance tomography (ERT) is a new geophysical imaging technique which can be used to map subsurface liquids as flow occurs during natural or man-induced processes and to map geologic structure. Man-induced processes such as tank leaks and clean-up processes such as steam injection can create changes in a soil's electrical properties that are readily measured. Electrical resistance tomography is a technique for reconstruction of subsurface electrical resistivity. The result of such a reconstruction is a 2 or 3 dimensional map of the electrical resistivity distribution underground made from a series of voltage and current measurements from buried electrodes. The ERT approach we follow here relies on detection and mapping of the changes in electrical resistivity associated with a leak.

ERT surveys are performed using a number of electrodes in boreholes and/or at the ground surface to image the resistivity distribution between two boreholes. Using an automatic data collection and switching system, we collect a few hundred electrical resistance measurements. The data is then processed to produce electrical resistivity tomographs using state of the art data inversion algorithms. We use these measurements to calculate tomographs that show the spatial distribution of the subsurface resistivities.

1.3 Description of 2D algorithms:

1.3.1 Finite element iterative algorithm

This algorithm involves solving both the forward and inverse problems. The forward and inverse algorithms used in this work are described in detail by LaBrecque et al. (1995); we summarize them below. The solution to the forward problem uses the finite element method (FEM) to compute the potential electrical response of a 2-D earth to a 3-D source. To avoid the difficulty of numerically solving a 3-D problem, Poisson's equation is formulated in the wave-number domain using the Fourier transformation in the strike (y) direction. The governing equation is:

$$\frac{\partial}{\partial x}\left(\sigma\frac{\partial V}{\partial x}\right) + \frac{\partial}{\partial z}\left(\sigma\frac{\partial V}{\partial z}\right) - \lambda^2\sigma V = -I\delta(x)\delta(z),\qquad(1)$$

where V is the potential in the Fourier transform domain, σ is the conductivity, λ is the Fourier transform variable, I is the source current, and $\delta(x)$ is the delta function (Hohmann, 1988). Our 2-D FEM algorithm is based on the theory described by Huebner and Thornton (1982), and our implementation of it follows that described by Wannamaker et al. (1987) for modeling 2-D magnetotelluric data.

Using the FEM, we can calculate the potentials for a discrete number of transform variables at the nodes of a mesh of quadrilateral elements. We can then transform the potentials back into the Cartesian domain using the method described by LaBrecque (1989). The boundary conditions are assumed to be Neumann (0 potential gradient, no vertical current flow) at the ground/air interface and Dirichlet (potential set to 0) along the other three boundaries.

The inverse algorithm iteratively finds the maximum value of the stabilization parameter α to minimize the objective function:

$$Y(\mathbf{P}) = \chi^2(\mathbf{P}) + \alpha W(\mathbf{P})\qquad(2)$$

gives a value of χ^2 (**P**) equal to an *a priori* value; here **P** is the vector of unknown parameters, W(**P**) is the roughness operator (Tikhonov and Arsenin, 1977), and χ^2 is the chi-squared statistic. In our work, the *a priori* value of χ^2 is assumed to be equal to the number of data points. The inverted parameters are the natural logarithms of the conductivities of *pixels*. Each pixel contains the elements of a rectangular region of a FEM mesh. The chi-squared statistic is given by:

$$\chi^2 = \left[\mathbf{D} - \mathbf{F}(\mathbf{P})\right]^{\mathbf{T}}\mathbf{W}^{-1}\left[\mathbf{D} - \mathbf{F}(\mathbf{P})\right],\qquad(3)$$

where **D** is the vector of known data values and **W** is the data covariance matrix.

The roughness operator stabilizes and removes ambiguity in the resistivity inversion by minimizing the model roughness; this is referred to as smoothest inversion. The roughness operator $W(\mathbf{P})$ is given by:

$$W(\mathbf{P}) = \mathbf{P}^{\mathbf{T}}\mathbf{R}(\mathbf{P});$$ (4)

here $\mathbf{R}$ is the roughness matrix, which is a numerical approximation to the 2-D Laplacian operator (Sasaki, 1992).

At the *ith* iteration, our algorithm begins by approximating the forward solution by a first-order Taylor's series of the form:

$$\mathbf{F}(\mathbf{P}) = \mathbf{F}(\mathbf{P}_i) + \mathbf{A}(\mathbf{P} - \mathbf{P}_i),$$ (5)

where **F(P)** is the forward solution, **A** is the sensitivity matrix and $\mathbf{P}_i$ is the vector of estimated parameters at the *i*th iteration.

Using a root-finding algorithm, we estimate α for this linearized system. We then use a modified Marquardt method iteration (Bard, 1974) to find the parameters that minimize the objective function [(Eq. (2)] for the estimated value of α. Iteration is repeated until the changes in α and χ^2 from one iteration to the next are suitably small.

1.3.2 Single pass image reconstruction:
The computational demands and potential convergence failure of a formal inverse solution such as that above has prompted the development of a number of image reconstruction algorithms which are purely qualitative. We adopt here a version of the one such algorithm of Kotre(1989) which computes a 'gray scale' associated with each element j =1,2,...m according to a simple matrix - vector product:

$$P_J = \sum_{i=1}^{n} S_{i,j} \ln(T_i' / T_i) \qquad J = 1,2,....m$$ (6)

where n is the number of independent measurements T_i and T_i' are the ith measured boundary transfer resistances before and after a change in resistivity within the region. $S_{i,j}$ is a sensitivity coefficient for element j and independent measurement i derived in the same manner as the smoothness algorithm in the previous section.

The sensitivity matrix is computed on a finite element mesh with uniform resistivity. Since no inverse matrices are required the algorithm is computationally efficient and very fast as only one matrix vector product is required for each image.

1.4 Description of 3D algorithm:
Our 3-D inversion algorithm requires a forward solution which can numerically solve the potential equation:

$$\frac{\partial}{\partial x}\left(\sigma \frac{\partial}{\partial x} V\right) + \frac{\partial}{\partial y}\left(\sigma \frac{\partial}{\partial y} V\right) + \frac{\partial}{\partial z}\left(\sigma \frac{\partial}{\partial z} V\right) = I(x, y, z), \quad (7)$$

where V is the scalar electrical potential and I(x,y,z) is the distribution of electrical current sources and sinks. We use the finite element method (FEM) with rectangular, hexahedral elements (Pridmore et al., 1981) to convert the differential equation (1) into a system of linear equations. This system of equations is then solved iteratively using the diagonally-weighted preconditioned-conjugate-gradient method (Pini, G., and Gambolati, G., 1990). The forward modeling algorithm is a modified version of one written by Qin (1995). The boundary conditions are assumed to be Neumann (0 potential gradient, no vertical current flow) at the ground/air interface and Dirichlet (potential set to 0) along the other five boundaries.

3-D inversion is by nature strongly underdetermined and so inverse solutions which consider only the fitting of the forward model to field data are non-unique. Therefore, we implemented a regularized solution (Tikhonov and Arsinen, 1977) which jointly minimizes the misfit of the forward model to the field data and stabilizes the inverted value of the parameters. To find the optimal value of the parameter vector **P**, our algorithm finds the maximum value of α, the stabilization parameter, for which minimizing:

$$Y(\mathbf{P}) = \chi^2(\mathbf{P}) + \alpha \; \mathbf{P}^T\underline{\mathbf{R}}\mathbf{P} \qquad (8)$$

gives

$$\chi^2 (\mathbf{P}) = \chi^2_{\text{a-prior}} . \qquad (9)$$

In equation 8, we have chosen to use, $\underline{\mathbf{R}}$, the solution roughness, as the stabilizing functional. This is approximated by:

$$\underline{\mathbf{R}} = \underline{\mathbf{x}}^T\underline{\mathbf{x}} + \underline{\mathbf{y}}^T\underline{\mathbf{y}} + \underline{\mathbf{z}}^T\underline{\mathbf{z}} \; , \qquad (10)$$

where $\underline{\mathbf{x}}$, $\underline{\mathbf{y}}$, and $\underline{\mathbf{z}}$ are the first order difference operators in the X , Y , and Z directions. Also in equation (9), $\chi^2_{\text{a-prior}}$ is equal to the number of data points and χ^2 is given by:

$$\chi^2 = (\mathbf{D} - \mathbf{F(P)})^T\underline{\mathbf{W}} (\mathbf{D} - \mathbf{F(P)}) \qquad (11)$$

where **D** is the vector of known data values, **F(P)** is the forward solution and $\underline{\mathbf{W}}$ is a data weight matrix. The diagonal elements of $\underline{\mathbf{W}}$ are the reciprocals of the data variances and the non-diagonal elements are zero. This assumes non-correlated data errors.

The parameters, **P,** are the natural logarithms of the conductivity of the FEM elements. In the foreground (the part of the FEM mesh between the boreholes and near the boreholes) each parameter corresponds to a single finite element. In the background (the region away from the boreholes) we lump several finite elements together into a single parameter.

The nonlinear inversion is carried out iteratively as:

$$\mathbf{P}_{k+1} = \mathbf{P}_k + \Delta\mathbf{P}_k \; , \qquad (12)$$

where $\mathbf{P_k}$ is the vector of parameters from the previous iteration and $\Delta\mathbf{P_k}$ is the parameter change vector. $\Delta\mathbf{P_k}$ is found by solving the linear problem:

$$\Delta\mathbf{P_k} = \left(\underline{\mathbf{A}}_\mathbf{k}^\mathbf{T}\ \mathbf{W}\ \underline{\mathbf{A}}_\mathbf{k} + \alpha\underline{\mathbf{R}}\right)^{-1}\left(\underline{\mathbf{W}}\ \Delta\mathbf{D_k} - \alpha\mathbf{R}\ \mathbf{P_k}\right), \quad (13)$$

where $\underline{\mathbf{A}}_k$ is the sensitivity matrix and $\Delta\mathbf{D_k} = \mathbf{F}(\mathbf{P}) - \mathbf{D}$. The elements of the sensitivity matrix, $a_{i,j}$, are:

$$a_{i,j} = \frac{\partial\ F_i(\mathbf{P_k})}{\partial p_j} \quad (14)$$

where p_i is the ith element of $\mathbf{P_k}$ and $F_i(\mathbf{P_k})$ is the forward solution for the ith data point. Solving equation (13) exactly is not practical since the system is very large (50 000 by 50 000), full, and ill-conditioned. Instead, we use the conjugate-gradient method described by Mackie and Madden (1993) to give a stable, approximate solution to this linear system. The details will not be repeated here, but note that the solution does not require the calculation of the full sensitivity matrix. It requires only the calculation of the sensitivity matrix and its transpose multiplied by a vector.

Our routine differs from Mackie's in three ways. First, we use a method similar to that described by Rodi (1977) to calculate $\mathbf{A}^\mathbf{T}\ \mathbf{u}$ and $\mathbf{A}\ \mathbf{v}$ where $\mathbf{u}, \mathbf{v}$ are vectors. Since we calculate a forward model for every electrode, this method does not require any additional forward solutions during the conjugate gradient iterations. Second, we use more conjugate gradient iterations than Mackie and Madden (1993). For the magnetotelluric inverse problem, Mackie and Madden found that the non-linear inversion routine converged well with three conjugate gradient iterations. We usually require between 10 and 40 conjugate gradient iterations to achieve adequate convergence. Third, we use smoothness instead of comparison with an a-priori model to stabilize the inverse solution.

We have found that choosing the correct value of α is critical for both achieving rapid convergence of the non-linear inversion and for finding a good final parameter estimate. With our method, a new value of α is estimated at the end of each non-linear iteration. The estimate uses the assumption that the relation between χ^2 and α can be approximated by the rational function:

$$\chi^2 \cong \frac{b\ \alpha}{\alpha + a}, \quad (15)$$

where a and b are constants. The constant, b , is the value of χ^2 for a homogeneous half-space. The constant, a, is estimated from the values of a and χ^2 of the previous iteration. If the misfit is χ_k^2 and the desired misfit is χ^2_{target}, then the new estimate of α, α_{k+1} is:

$$\alpha_{k+1} = \frac{\dfrac{b}{\chi_k^2} - 1}{\dfrac{b}{\chi_{\mathbf{target}}^2} - 1}\, \alpha_k .\qquad (16)$$

The value of χ^2_{target} is chosen as the larger of $\chi^2_{\text{a-priori}}$ and $\chi^2_k / 2$.

Although the approach is simplistic, it usually converges to the correct value of χ^2 in 10 to 20 iterations.

2.1 Geologic setting:
The following geologic description is based on geological information presented in a report by Reidel et al., (1992). The test site used for this work is part of the 200 East Area in the Hanford Site, located near Richland, Washington. The near surface sediments at the test site and throughout the Hanford Site were deposited during periods of Pleistocene cataclysmic flooding and Holocene eolian activity. The cataclysmic flooding occurred when ice dams in western Montana and northern Idaho were breached, allowing large volumes of water to spill across eastern and northern Idaho. The floods created a variety of deposits, including giant flood bars.

The test site is underlain by the Hanford formation, which includes one of the cataclysmic flood bars. The Hanford formation consists of pebble to boulder size gravel, fine to coarse grained sand, and silt. This formation is thickest in the vicinity of the 200 West and 200 East Areas where it is up to 65 m thick. The near surface sediments at the test site consist primarily of fine to coarse grained sand displaying plane lamination and bedding. Paleocurrent indicators within beds of plane laminated sands are unidirectional, generally toward the South and East. Hydraulic conductivities for these sediments depend upon the silt content, which is variable.

2.2 Description of Experimental Site:
The field experiments were performed under a 15.2 m diameter steel tank mockup located at the Hanford Reservation (200 East Area). Figure 2 shows the layout at the leak detection experiment site. This empty steel tank contained several built-in spill points (two of which are shown). Sixteen boreholes with eight electrodes in each surrounded the tank. The electrodes were located in 10.7 m deep boreholes starting at the ground surface and spaced every 1.52 m. The diametrical distance between boreholes was 20.7 m.

This report covers the results obtained during two brine release experiments conducted from 7/25/94 to 7/31/94 and from 3/7/95 to 5/11/95 at the leak test facility. About 3800 liters of saline solution were released along a portion of the tank's edge (side release point in Fig. 2) and another 1900 liters were later released near the tank's center (center release point in Figure 2). The release rate averaged about 26 liters/hour (7 gallons/hour) for the side leak and about 3.2 l/hour (0.85 gals/hour) for the center leak. The ERT measurements were made using a pole-pole approach. A third release experiment was conducted using a spill point located halfway between the edge and the center of the tank. These results are not discussed here; experimental problems with the brine release system make these results inconclusive.

ERT images were made before, during and after the brine release in each of 8 horizontal planes beneath the tank. Plane 8 is a horizontal cross section at the ground surface 1.5 m above the bottom of the tank (so it contained the tank itself). Plane 7 is 1.5 m lower, a cross section level with the tank bottom. Plane 6 is 1.5 m below the tank bottom and so on to plane 1 which is 10.7 m below the ground surface. This arrangement provided a series of 2D image planes at many levels which, when assembled together, gave an overall 3D view of the plume formed beneath the tank during the release and which could be used to determine the effects of imaging current shunted through the tank bottom.

2.3 Image resolution and sensitivity--computer simulations:
We have performed computer simulations to investigate possible effects the tank may have on the approach and to investigate image resolution and sensitivity. The location of electrodes, distances, and soil properties used in the simulations matched those present at the experimental site; also the finite element meshes used were identical to those used to process the field data. The data used for these simulations was calculated using the forward solver in the three dimensional code described in section 1.4. The 3D resistivity structure assumed by the forward solver included a metallic tank. The forward solver calculated data for the case where a metallic tank was partially buried in soil with homogeneous resistivity of about 300 ohm-m (represents the pre-release situation). Data were then calculated for the case where the soil resistivity along a vertical column of elements below the tank changed to 10 ohm-m. This thirty-fold contrast represents the expected change caused by a brine release.

To simulate long term monitoring of a tank, we compared two sets: 1) a data set calculated for the case where a plume caused by a tank release is present, and 2) a corresponding data set calculated for the case where there is no plume. One may consider performing the analysis by subtracting, pixel by pixel, images without the plume anomaly beneath the tank from those with the plume. However, this approach cannot be used because the two dimensional reconstruction algorithm will not converge using input data for which the boundary conditions are clearly three dimensional--the earth surface and the tank bottom are not accounted for in the forward model of the 2D code. Therefore, the comparison was performed by inverting the quantity

$$\frac{R_a}{R_b} \times R_h \qquad (17)$$

where R_a is the transfer resistance calculated assuming a 3D resistivity model for the case after the release (3D model includes an electrically conductive tank and the plume beneath it), R_b is the transfer resistance calculated using a 3D model for the case before the release (3D model includes a conductive tank in an homogeneous half space) and R_h is the calculated transfer resistance for a model of uniform resistivity. The transfer resistance is simply the ratio of voltage to current for an individual 4 electrode measurement. This comparison is a simple perturbation from the uniform resistivity case as described by Daily and Owen (1991).

Figure 3 shows the variation in the resistivity ratio as the anomaly changes position from the edge of the tank (left column of images to the tank's center (right column of images). Note that the resistive anomaly in the model begins at the elevation of the second plane, extends vertically below the elevation of the bottom image plane and is one element wide and two elements deep. The results show that when the simulated vertical leak is at the center the magnitude of the reconstructed anomaly is smallest. Also, the width of the anomaly is exaggerated when the leak location is near the center. For a given anomaly position, the largest reconstructed changes (and

the changes closest to the true model) are generally observed on those planes farthest from the tank (bottom planes). This clearly means that sensitivity to an anomaly of a given magnitude and size depends strongly on the position of the anomaly relative to the locations of the sensing electrodes and the tank. Sensitivity is greatest near the electrodes or away from the tank (bottom planes) and lowest away from the electrodes or near the tank (upper planes).

These results also suggest that the data ratio technique described above can yield reasonable results in spite of the fact that neither the ground/air interface nor the tank are included in the 2d model. This analysis technique partially removes the effects of any part of the resistivity structure which does not fit the numerical model used in the forward calculation. These observations are verified by the field results discussed in Section 3.0.

An interesting question is, "how much of an effect does the presence of the metallic tank have on the observed results?". To evaluate this question, we repeated the analysis of the rightmost column of images in Figure 3, after removing the tank from the resistivity structure assumed by the forward solver. A comparison of "tank present" and "tank absent images" is shown in Figure 4 for the case of a column leak below the center of the tank. This figure shows that both the "tank present" and "tank absent" images show lower contrast anomaly than the model. Also, the width of the anomaly is significantly exaggerated in both cases. Figure 4 suggests that a significant fraction of the decreases in sensitivity observed in Figure 3 are related to the presence of the tank. Note that the "tank absent" images are significantly closer to the true model magnitude. These observations imply that the presence of the tank does have an effect on the observed resistivity ratios which tends to reduce sensitivity to changes related to a leak.

2.4 Experimental procedure--field test:
The first brine release experiment involved the easiest conditions for leak detection with ERT -- the brine was released along the sides of the tank where high sensitivity to the release was expected. In a second brine experiment, conducted in March and April, 1995, brine was released near the tank's center which presented more difficult detection conditions because this is a region of minimum sensitivity.

The first brine release was along the side of the tank (NE quadrant) over a 7 ft. length ("side leak" in Figure 1). The fluid was a 0.08 molar sodium chloride solution (approximately 7 Kg./1000 liters of water). This amount of salt increased the conductivity of the solution from about 0.03 to 3.0 S/m. We note that this concentration should be much more dilute than real Hanford tank liquids which are typically fully saturated solutions. For example, a fully saturated sodium nitrate solution would require an 8.4 molar concentration which is about 100 times more concentrated than the brine concentration used for the test. This lower concentration should make the test brine substantially harder to detect than the real tank brines. The second brine release was conducted from a point just a few inches below the tank's bottom at the center ("center release" in Figure 2).

ERT images were made before, during and after each brine release in each of 8 horizontal planes beneath the tank. The image planes are numbered from the bottom to the ground surface. Plane 8 was a cross section at the ground surface 1.5 m above the bottom of the tank (so it contained the tank itself). Plane 7 was 1.5 m lower, a cross section level with the tank bottom. Plane 6 was 1.5 m below the tank bottom and so on to plane 1 which was 10.7 m below the tank bottom. This arrangement of image planes provided a series of detailed images at many levels which, when assembled together, gave an overall view of the plume formed beneath the tank during the release.

3.0 Discussion of Results:

3.1 Side release, two dimensional tomography results:
Figure 5 presents two-dimensional (2D) tomographs collected during the course of the side release experiment. The location of the release point is indicated on the figure. The images show which areas of the soil changed in response to the brine spill. Each column of images shows the changes detected for a given time at various depths; the depth of images on each column increases from top (0 m. depth to bottom (10.7 m depth). Time and leaked volume increase from left to right on the figure. The images for July 26 at depths of 1.5 and 3 m (the top two available images of the first column in Figure 5; the top two planes were not collected at this time) show clearly detectable electrical conductivity increases directly below the release point close to the "path for vertical migration". This behavior suggests that the brine is moving almost straight down as may be expected in reasonably homogeneous sandy soil present at the experimental site. Note that the changes observed increase in magnitude as time and spilled volume increase. Also, note that the bottom of the changing region deepens as time increases.

Electrical noise measurements were also made during the tests by comparing each measurement with its reciprocal. These measurements where then used to calculate reconstructions which showed the magnitude of changes in the images expected from measurement error. The worst case of these "noise" images showed the resistivity ratio to deviate from 1.0 (i.e., perfect result when no changes occur) by +/-0.005. This analysis shows that resistivity changes shown in Figure 5 are much bigger (resistivity ratios are much smaller) than those changes which could be expected due to measurement error. The analysis assumes that the differences between the normal and reciprocal measurements provide good estimates of the measurement errors.

The results obtained early during the side release show that reliable changes associated with the leak were detected after 190 liters (50 gals.) had been released. These results are not shown in Figure 5 due to space limitations. Note that data was not collected when the released volume was smaller than 190 liters. It is possible that volumes smaller than 190 liters are detectable.

The results in Figure 5 were obtained using the iterative algorithm described in Section 1.3.1. Figure 6 shows some results from the side release obtained using the simpler "single pass" algorithm, described in Section 1.3.2. Note that the color scale in Figure 6 is qualitative. A comparison of Figures 5 and 6 shows that both tomograph sets show anomalies close to the "path for vertical migration" that the leak would follow in a homogeneous medium. However, the anomalies in 5 are more centered on the path for vertical migration than the anomalies in 6. The shapes of the anomalies are also somewhat different. This comparison suggests that both algorithms yield results which are in coarse agreement even though the results in 6 are generated with a much simpler algorithm than those in 5.

Although there are no corroborating data, the images in 5a and 5b are consistent with the behavior expected for infiltration of water released into a fairly homogeneous unsaturated soil. There is a clear decrease in resistivity of the volume directly below the release point from which the plume appears to drain downward by gravity and spreads laterally by capillary suction and as it encounters soil heterogeneity. The approximate leak location can be estimated as the point directly above the region of maximum change in the top few planes. The lateral and vertical extent of the plume as a function of time can also be roughly estimated from the images. The aggregate of these results is consistent with intuition. We maintain that, in the absence of independent

corroborating data, this fact supports the hypothesis that the tomographs are credible representations of the released brine.

3.2 Side release, three dimensional results:
Figure 7 shows three dimensional ERT tomographs generated from data collected during the side leak. In this case, the data are used to calculate the resistivity changes within a block underneath the tank (instead of as a series of two dimensional slices shown in Figure 2) using only data from electrodes located at 1.5 m, 6.1 and 10.7 m depth.

The three dimensional inversion explicitly accounts for the metal structure. This is in contrast to our attempts to remove the effects of this conducting boundary as we did in the 2d inversions. Thus, one may expect that the 3D results are more accurate than the 2D results. However, the calculation times for the 3D inversions are about 40 times longer than for the 2D inversions covering the same volume.

It is necessary to calculate the electric field near the metal-soil boundary during forward modeling by the 3D code. In order to estimate the resistivity values for the elements within the tank volume, we assumed that the resistance-thickness product for the steel layer equaled the resistance-thickness product for the elements. We first calculated the resistance expected from the 0.00635 m (1/4 in.) layer of steel that makes up the tank sides. The resistivities of all the elements within the tank volume were then set to 10^{-3} ohm-m; these elements were kept fixed at this initial value during the inversion.

The resistivity contrast between the soil and the metal can be as high as 10^8; for comparison, normal geologic systems have contrasts which are about 10^2. The large resistivity contrast across these layers requires that accurate forward solvers be used to obtain accurate calculation of the electric field. However, the inverse problem is regularized, meaning that inversion finds the smoothest resistivity structure which fits the data to some tolerance. The algorithm will tend to find resistivity models where there is minimal contrast between an element and its neighbors. It is necessary to modify the inversion algorithm because of the tank and soil. Otherwise, the resistivity associated with the tank will be "smeared" to the surrounding elements representing the soil and yield erroneous values. The algorithm used for this inversion was modified to allow for a non-smooth solution at the tank boundary.

The 3D reconstruction shown in Figure 7, is 21.3 m wide, 21.3 m. long and 10.7 m. tall and is the reconstructed volume bounded by the electrode arrays in the sixteen holes around the tank. Those parts of the reconstruction with resistivity differences smaller than 150 ohm-m are shown as transparent so that the interior of the block can be observed. Note that the 2D reconstructions in Figure 5 and 3D images in Figure 7 show the same approximate position, shape and size of the anomaly over time. The 3D images may provide a better view of the changes caused by the leak because: a) the flow regime is truly three-dimensional, so there is no need to assume that the resistivity extends to infinity in the third dimension, b) there is no need for interpolation between adjacent 2D slices, and, c) the effect of the metallic barrier is explicitly accounted for in the 3D images but not in the 2D images. However, the 3D images takes much longer to calculate (5-6 days per block) than the 2D images (20 minutes per slice).

3.2.1 Tank used as an electrode:
The modeling cases shown previously suggest that the position of the anomaly has a significant effect on the results observed. Changes below the tank's center are observed with much less

sensitivity than changes near the side of the tank. The modeling results suggest that anomalies closer to the electrodes are observed with greater sensitivity. If the tank itself is used as one large electrode, it may offer increased sensitivity to the leak because it is located closer to the leak point than any other electrode.

Figure 8 illustrates the effects of using the tank as an electrode. The figure compares two resistivity difference tomographs. The one on the left shows the results when only hole to hole data is used. The right image in Figure 8 shows the results when the tank is used in combination with the boreholes electrodes, i.e., hole to hole measurements and hole to tank measurements were used in combination. The difference image on the left of the figure is more elongated than the image on the right, which is more spherical. We do not have independent data that can be used to determine which of the two results is closer to the true structure. However, we speculate that the image on the right may more closely represent the true structure because the spherical shape is closer to what may be expected for a reasonably homogeneous sandy soil such as what exists at the experimental site.

3.3 Center Leak, two dimensional results:
Figure 9 presents two-dimensional (2D) tomographs collected during the course of the center release experiment (spill point location shown in Figure 2). Time and leaked volume increase from left to right on the figure. The images for March 11 show clearly detectable electrical conductivity increases below the release point and extending to the South and East. The changes observed increase in magnitude as time and spilled volume increase just as was observed during the side release. Also, note that the bottom of the changing region extends deeper as time increases. This behavior suggests that the brine is moving mainly down with some movement to the SE. The movement to the SE may be explained by the slight SE dip of the sand layers at the site.

We suspect that some of the images in Figure 9 are distorted. For example, note the images at 1.5 and 3.0 m depth on 5/10/95. These images suggest that the whole region between the boreholes has decreased in resistivity; we believe that the width of the anomaly has been greatly exaggerated in these cases due to the minimal resolution to targets located just below the tank near the image center. Also, anomaly distortions can be expected when the horizontal image plane is in close proximity to the tank.

Electrical noise measurements were also made during the center release test. The results from these tests showed the same noise effect on the image as observed during the side release, i.e., ratios larger than 0.995 could be caused by noise. The resistivity ratios shown in Figure 9 are much smaller (i.e., represent larger changes) than those changes caused by measurement error. Note that resistivity ratios of approximately 0.94 were observed on 3/11 after 193 liters (about 50 gallons) had been spilled. These results imply that volumes of brine larger than 190 liters released from the center of the tank should be readily detectable, when site conditions are similar to those at the test site.

3.4 Center leak results--three dimensional tomographs:

3.4.1 Using metal cased boreholes as long electrodes:
Some of the metal tanks at the Hanford site are surrounded by metal cased vertical boreholes (Cruse et al., 1995). These boreholes are used to conduct gamma radiation surveys to detect radioactive contamination leaking from a tank. One approach considered in our work is to use these metal cased boreholes as long electrodes for ERT leak detection. If successful, this

approach would reduce the need to drill new boreholes for electrode installation resulting in significant cost savings because of the high cost of drilling into potentially contaminated and radioactive soil.

The test site described in Section 2.2 and Figure 2 was modified to create an electrical analog to a tank surrounded by 4 metal cased boreholes and 4 normal ERT electrode boreholes. To approximate a metal cased borehole, the eight electrodes in an ERT borehole were shorted together, creating a piecewise continuous electrode between the top and bottom electrode. Every other ERT hole was used as a "metal casing analog". Three dimensional resistivity surveys were then conducted using four normal ERT boreholes and four 'metal casing analogs'. The data were inverted using the 3D resistivity algorithm and the "metal casing analogs" were modeled as vertical columns of highly conducting elements which extended from the ground surface to 10.7 m depth.

Figure 10 shows the resistivity differences obtained when four "metal casing analogs" along with four normal electrode boreholes (with eight electrodes in each borehole) were used during the center release. Note that two vertical slices are shown crosscutting the reconstructed block; elements with values between 0 and -400 ohm-m are transparent. The top tomograph in the figure shows the resistivity differences observed as a result of noise data only. That is, the tomograph calculated using normal data was subtracted from the tomograph using reciprocal data. The lower two tomographs show the resistivity differences observed at two times during the leak. Note that resistivity is decreasing below the leak point and the anomaly extends laterally as well as downward. The changes observed in the later two tomographs are substantially greater in magnitude and in size than those in the earlier tomograph, implying that the images represent a growing brine plume beneath the tank. These results also suggest that metal cased boreholes used as long electrodes, in combination with normal ERT electrodes, can be used to save drilling costs for ERT data collection.

Three features of the images in Figure 10 are probably erroneous. First, there are vertical anomalies at the North, East, and South positions. These features coincide with the metal casing analogs and may indicate that the metal casing analogs are poorly approximated by the coarse finite element mesh model we used. Second, the resistivity difference anomaly in Figure 10 is widest just below the tank and narrows with depth. We suggest that the width of the anomaly is exaggerated close to the tank and that the width gets closer to the true width with increasing depth. The metal structure diminishes resolution close to the tank due its extremely low electrical resistivity. Thus, the width of the anomaly is "smeared" or exaggerated. Third, the resistivity differences observed are higher than those observed when only point electrodes are used (for example, refer to figures 7 and 8 for the side release). This difference is not understood; we suspect that the coarse approximations used to model the "metal casing analogs" may have caused the exaggerated resistivity differences.

3.4.2 Three dimensional resistivity ratio inversions:
The three dimensional resistivity differences shown in Figures 7 and 8 required 5-6 days of CPU time per image. Most of the time expense was caused by the large resistivity contrasts between soil and metal, which resulted in an excessive number of forward solver iterations. In an attempt to reduce the time required for 3D inversions, we chose to invert resistance ratios. When resistance ratios are inverted, the forward solver does not have to calculate the potential field for high resistivity contrasts. Inversion of resistance ratios reduced the time required for inversion from 5-6 days to 2-3 days.

The 3D resistivity ratio results are shown in Figure 11. Note that the smallest resistivity ratios are located directly below the leak point. Also, the ratios get smaller in magnitude and penetrate deeper as the leaked volume and time increased. Close to the tank bottom, the width of the leak anomaly is exaggerated because of the effects of the metal barrier on resolution. The 3D ratios in Figure 11 are generally consistent with the center release 2D ratios in Figure 9. However, the 3D ratios should provide a more accurate result because the distortion effects created by mapping a 3D structure unto a 2D image should be large in Figure 9 (2D results) and small in Figure 11 (3D results).

The 3D ratios results of Figure 11 (1200 liters released) are consistent with the corresponding 3D resistivity differences shown in Figure 10 (data collected using point electrodes and "metal casing analogs"). Note that the shape, size and location of the anomalies is similar. The behavior as a function of time is also similar. These figures show that the tomographs using eight "metal casing analogs" and point electrode boreholes are similar to the tomographs using 16 point electrode boreholes.

4.0 Implications Of Field Test Results:

The results to date indicate that these electrical methods can be used to address key questions pertaining to leak detection. We can use the field experiment results described above to extrapolate how these electrical methods can be used for leak monitoring under metallic tanks. These extrapolations are made assuming conditions similar to those used during the tests, i.e., same number of boreholes and electrodes, similar borehole separations, and similar contrast between the spilled liquid and the soil. The approach requires that an active tank leak change the soil's resistivity in order to be detected; this resistivity change is established by repeating the ERT surveys over a period of time. Note that this approach will not work for pre-existing plumes which have stopped moving because no detectable changes in resistivity would develop.

The field experience indicated that ERT has some positive attributes for leak detection. The approach is well suited for long term monitoring because it can be easily automated. The use of stationary electrodes (instead of movable probes) means that a system that can automatically switch between the various electrodes can be used to collect the data with minimal field personnel. The measurements can be made in a reasonably short period of time (data collection using all the electrodes at the experimental site could be completed in about 4 hours). The processing time for 2D data inversions was approximately 20 minutes per plane (using a Sun SPARC10 workstation); Ramirez et al, 1995, showed that 2D data processing can be done automatically in near real time (tomographs available within 20 minutes of data collection). For 3D absolute resistivity inversions, the processing time was typically 5-6 days (assuming data from 16 boreholes is used). For 3D resistivity ratio inversions, the processing time was typically 2-3 days. Additional improvements in the 3D algorithm may reduce the processing time to about 1 day.

The resistivity change tomographs can be used to address the following questions.

1) Is there a leak?
In the tests we performed, liquid volumes equal to or larger than roughly 190 liters (50 gallons) can be reliably detected when the water is released over a short sector of the tank (approximately 3 m or less). This detection threshold appears to be approximately the same for both a side release and a release from the tank's center. It is possible that the detection limit is lower than 190 liters because no data were collected at times when the spilled volume was smaller.

ERT can provide complementary information if used with in-tank liquid level measurements. For example, during periods of active sluicing the water level in the tank is oscillating such that the in - tank liquid level sensors cannot be used; the ERT detection approach could supplement the liquid level sensors during this time. During periods where the water level is stable, these two methods used in combination can help verify each other's results.

For leakage from a single point, the detection limits for ERT are better than the detection threshold allowed by the accuracy of currently-used in-tank liquid level measurements of 2.54 cm inches (or about +/-10,000 liters)(Cruse et al., 1995) for a 23 m diameter tank. For a distributed leak (i.e., small leak rates from many holes located over a broad area of the tank) the detection threshold using ERT can only be estimated based on the results of the "single point release" experiments conducted.

One way to estimate the detection threshold for a distributed leak is to assume that the ratio of liquid volume spilled to anomaly size is the same for both a single point release and a distributed release. We will assume that the distributed leak is caused by multiple holes, evenly spaced around all of the tank's perimeter. The liquid volume to anomaly size ratio can then be used to make a coarse estimate of the spilled volume required for detection. We calculated this ratio for the case where the measured resistivity change caused by the leak was 10 % or larger and the total spilled volume was 570 liters; note that the case chosen is conservative because it involves a volume 3 times larger than the 190 liters that can be detected for a single point release. We then estimated that the area covered by a distributed leak anomaly spreading around the tank's perimeter would be about 8 times larger than that of a single point release. Thus, the detection threshold for a distributed leak is estimated to be 8 times larger than for a single point release, or 4600 liters. We consider this a rough estimate that needs to be verified in future experiments.

From the results of this work, we can estimate the capacity of ERT to detect leakage from a tank of non-aqueous liquids. Noise analyses in section 3.3 show that resistivity changes from measurement error would cause changes no larger than 0.5 %. We assume that the noise analysis sets a lower bound on the minimum magnitude of resistivity change that is detectable; we also assume that the minimum resistivity change which can be detected reliably has to be four times as large (2%) than the changes that can be expected to be caused by noise. This also means that, for liquids other than salt water, a leak volume sufficiently large enough to cause a 2.0% (or larger) change in resistivity may be required.

2) Where is the leak located?
The field results and the numerical models showed that, for a single point release, the images could be used to approximately locate the leak point when the liquid moves straight down. When the region of maximum change in the image is used, we estimate that the leak point can be located with an accuracy of about one element width (2.5 m) for a side release and two element widths (5 m) for a center release. For a distributed leak, the ability to locate the individual leak points will depend on several factors including the separation between leak points and the soil volume affected by each.

3) Can the migration of the plume be monitored?
The ERT tomographs clearly showed the downward and lateral migration of the released liquid. This information can be used to support remedial action that would follow a spill such as temporary

barriers to contain the spreading contamination or extraction wells that would remove the soil contamination.

4) Can the user reliably distinguish between resistivity changes caused by a leak and changes caused by unrelated phenomena such as electrical noise?

Electrical noise measurements were made during the test. These measurements were then used to calculate tomographs that defined the magnitude of change as a result of electrical noise. The analysis showed that electrical noise was not a limiting factor when detecting leaks during the test. Only changes which are larger than those shown in the noise images were interpreted as related to the leak. If a similar approach was used during monitoring operations, the user could reliably distinguish between changes associated with a leak and those caused by measurement error.

The effects of rain on the soil at the test site were also evaluated during the course of the work as several rainstorms affected the experimental site while measurements were being made. Rain water infiltration caused no detectable changes in any of the tomograph planes.

The long term stability and accuracy of the measurement instruments needs to be verified in order to insure that instrument drift does not result in false changes. Instrument stability and accuracy can be verified in the field on a periodic basis using calibrated resistors. This calibration check verifies that the instrument accurately measures the resistance of a known resistor and also verifies that the instrument returns stable measurements over long time periods.

4.1 Number of boreholes needed to detect spills:
For electrical imaging under a steel tank to be sensitive to the presence of fluids leaving the tank, the measurement electrodes must be near or below the bottom of the tank. When the tanks are located at the surface, the electrodes can be installed along the ground surface or in shallow boreholes. For tanks located well below ground surface, boreholes are required for electrode installation.

For the case of buried tanks such as those at Hanford, the electrode array, to be deep enough, must be installed in boreholes. Drilling is expensive and at Hanford is discouraged because of the risk of penetrating contaminated soil. The leak test results can be used to illustrate the effects of some strategies which minimize the need for drilling to emplace ERT electrodes. Figures 12 and 13 compare the 2D tomographs from the side release (Fig. 12, approximately 3900 liters spilled) and the center release (Fig 13, approximately 1000 liters released). The figures contrast the results obtained when data from all the boreholes (16) are used (left column of images, the results obtained with data from only 8 boreholes (middle column), and the results obtained with data from only four boreholes (right column).

The side release results in Figure 12 show the largest change magnitudes when 16 boreholes are used and the smallest magnitudes are observed with four. We conclude that, within the limits of the test, the sensitivity of the technique to the leak increases with the number of boreholes used. The figure also shows that even with only four boreholes the changes resulting from the leak can still be detected and located. There is also a correlation between the number of boreholes used in the inversion and the spatial extent of the plume imaged. We conclude that the image resolution is also affected by the number of boreholes. These results imply that there will be a tradeoff between the number of electrodes around the tank and the desired sensitivity and resolution with which the leak can be detected.

Even the planes at 0 and 1.5 meter can detect and roughly resolve the leak. This implies that, for the case of surface tanks, it should be possible to monitor for leaks using surface electrodes. However, this approach would reduce the ability to track the movement of the plume in the subsurface.

The center release results in Figure 13 are generally consistent with those of the side release in that the magnitude of the leak induced anomaly gets smaller as the number of boreholes used decreases. The 16 borehole results (left column of images) and the 8 borehole results (center column of images) typically show the maximum changes (smallest resistivity ratio) very close to the vertical black line indicating the most likely path for the tracer; note that the black line is very close to the "bull's eye" formed by the image contours. However, the four borehole results (rightmost column) do not follow this pattern, sometimes, the smallest resistivity ratios are observed in other parts of the image (e.g., images at 4.6, 6.1, 7.6, and 8.1 m of depth). The results in Figure 13 suggest that, to preserve the ability to roughly locate a leak from the tank's center, more than four boreholes are needed and that the differences between 16 borehole results and 8 borehole results are relatively minor.

Monitoring for leaks in a practical setting requires a balance between the costs of additional boreholes and the added resolution and sensitivity that the extra boreholes would provide. Based on the field results shown, we suggest that a reasonable compromise between these competing requirements would make use of 6 to 8 boreholes. This approach would preserve enough sensitivity and enough resolution to be able to approximately locate the leak and to map the movement of the plume. Another approach is the use of horizontal wells to install electrodes beneath the tank. Although horizontal boreholes cost more to install, fewer may be needed.

5.0 Summary and Conclusions:

The results from two field experiments and from numerical simulations have been presented to illustrate the performance of ERT to detect leaks beneath a metal tank and to map the resulting plumes. The approach described here relies on detection and mapping of the changes in electrical resistivity associated with a leak. Many liquids released from tanks can create changes in a soil's electrical properties that are readily measured. Electrical resistance tomography is used as an inversion technique to map the soil's electrical resistivity in two and three dimensional space. Most 2D and 3D inversions discussed were performed using a finite element technique; some of the 2D data was also processed with a backprojection algorithm.

The field experiments were performed under a 15.2 m diameter steel tank mockup located at the Hanford Reservation, near Richland, Washington. This empty steel tank contained several built-in spill points from which controlled releases could be performed. Sixteen boreholes surrounded the tank; in each hole, eight electrodes were spaced every 1.52 m between 0 and 10.7 m depth. Brine, with a resistivity of 0.3 ohm-m, was released into soil of approximately 300 ohm-m resistivity to simulate the electrical properties of radioactive brine leaks from a high level radioactive waste storage tank. ERT surveys were performed before, during and after each brine release and two dimensional and three dimensional inversions were calculated. This report discusses the results obtained for a brine released along the tank's side and for a release directly below the tank's center.

Numerical modeling results show that the presence of the tank decreases the sensitivity to the leak induced changes, but that it should still be possible to detect the changes even below the tank's center. Modeling also shows that the width of the leak anomaly is exaggerated in all cases, particularly for anomalies near the image center. These modeling-based observations are consistent with the field results.

The 2D field results from both the side release and center release tests are consistent with the behavior expected for infiltration of water released into a fairly homogeneous unsaturated soil. There is a clear decrease in resistivity of the volume directly below the release point from which the plume appears to drain downward by gravity. For the side release, the approximate leak location can be found directly above the region of maximum change in the top few planes. The lateral and vertical extent of the plume as a function of time can also be roughly estimated from the images. The center release results are consistent with the side release; the primary difference is that the center leak anomalies are, in general, wider than those for the side leak due to decreased resolution near the images' center. In summary, these results show that ERT detected the brine released from both leak locations and could follow its downward propagation. The location, magnitude and time behavior of the anomaly observed during the brine spill is consistent with the hypothesis that the anomaly was caused by the leakage and not by unrelated phenomena such as electrical noise.

The 3D results from the side release show reasonable agreement with the 2D results. One advantages of 3D inversions is that large metal structures such as the tank itself and metal cased boreholes can be modeled and thus, used as electrodes. The field results suggest that metal cased boreholes may be used as electrodes in combination with point electrodes located in other boreholes and that this approach yields reasonable results. The field results also suggest that when the tank is used as an electrode (in addition to the borehole electrodes) improved resolution may be obtained.

By the time the first measurements during either spill had been made, the resistivity had changed approximately 5%, it may be possible that smaller changes are detectable. Noise analysis results suggest that it may be possible to see changes as small as 2%. The estimated number of boreholes needed for successful leak detection below a tank is roughly 6 to 8 boreholes; however, with fewer boreholes, there is diminished sensitivity to a leak.

6.0 Acknowledgments:

7.0 References:

Bard, Y., 1974, *Nonlinear Parameter Estimation* (Academic Press, New York), pp. 111–113.

Cruse, J., D. Iwatate, K. Tollefson, R. Treat, T. Trenkler, and R. Lewis, 1995, Functions and Requirements for Hanford Single-Shell Tank Leakage Detection and Monitoring, WHC-SD-WM-FRD-021, Westinghouse Hanford Co, Richland, WA.

Daily, W. and E. Owen, Cross Borehole Resistivity Tomography, *Geophysics*, *56*, 1228-1235, 1991.

Daily, W., A. Ramirez, D. LaBrecque and W. Barber, Electrical Resistance Tomography at the Oregon Graduate Institute Experiment, *J. of Applied Geophysics,* in press, 1995.

Kotre, C.J., 'A Sensitivity Coefficient Method for the Reconstruction of Electrical Impedance Tomograms', *Clin. Phys. Physiol. Meas.,* Vol. 10, p275-281, 1989.

LaBrecque, D. J., M. Milleto, W. Daily, A. Ramirez, and E. Owen, 1995, "The Effects of Noise on Occam's Inversion of Resistivity Tomography Data," *Geophysics,* in press.

LaBrecque, D. J., 1989, *Cross-Borehole Resistivity Modeling and Model Fitting,* Ph.D. thesis, University of Utah.

Hohmann, G. W., 1988, "Numerical Modeling for Electromagnetic Methods in Geophysics," in Nabighian, M. N., Ed., Electromagnetic Methods in Geophysics, 1: Soc. Expl. Geophys., Invest. in Geophys., no. 3, 313–363.

Huebner, K. H., and E. A. Thornton, 1982, *The Finite Element Method for Engineers* (Wiley, New York).

Mackie R. L., and Madden, T. R. 1993, Three-dimensional magnetotelluric inversion using conjugate gradients: Geophys. J. Int. **115**, 215-229.

Mosteller, F., and Tukey, J. W., 1977, Data analysis and regression: Addison-Wesley Publishing Company, 365-369.

Reidel, S. P., K. A. Lindsey, and K. R. Fecht, 1992, Field Trip Guide to the Hanford Site, WHC-MR-0391, Westighouse Hanford Corp., Richland, WA.

Pridmore, D. F., Hohmann, G. W., Ward, S. H., and Sill, W. R., 1981, An investigations of finite-element modeling for electical and electromagnetic data in three dimensions: Geophysics, **46**, 1009-1024.

Pini, G., and Gambolati, G., Is a simple diagonal scaling the best preconditioner for conjugate gradients on supercomputers?: Adv. water Resources, **13**, 147-153.

Qin, Jizeng, 1995, Three-dimensional DC resistivity forwared and inversion by finite element method: Ph. D. dis., University of Arizona, Tucson Arizona.

Ramirez, A., Daily, W. and R. Newmark, 1995, Electrical Resistance Tomography for Steam Injection and Process Control, *Journal of Enviromental. and Eng. Geophysics,* vol. 0, #1, pp39-51.

Rodi, W. L., 1976, A technique for improving the accuracy of finite element soutions for magnetotelluic data: Geohys. J. R. Astr. Soc., **44**, 483-506.

Sasaki, Y., 1992, "Resolution of Resistivity Tomography Inferred from Numerical Simulation," *Geophysical Prospecting* **40**, 453–463.

Tikhonov, A. N. and Arsenin, V. Y., 1977, Solutions of ill-posed problems, ed. Fritz, J., John Wiley & Sonss, New York.

Wannamaker, P. E., J. A. Stodt, and L. Rijo, 1987, *PW2D Finite Element Program for Solution of Magnetotelluric Responses of Two-Dimensional Earth Resistivity Structure,* DOE/SAN/12196-13, Univ. of Utah Research Institute, Earth Science Laboratory report ESL-158.
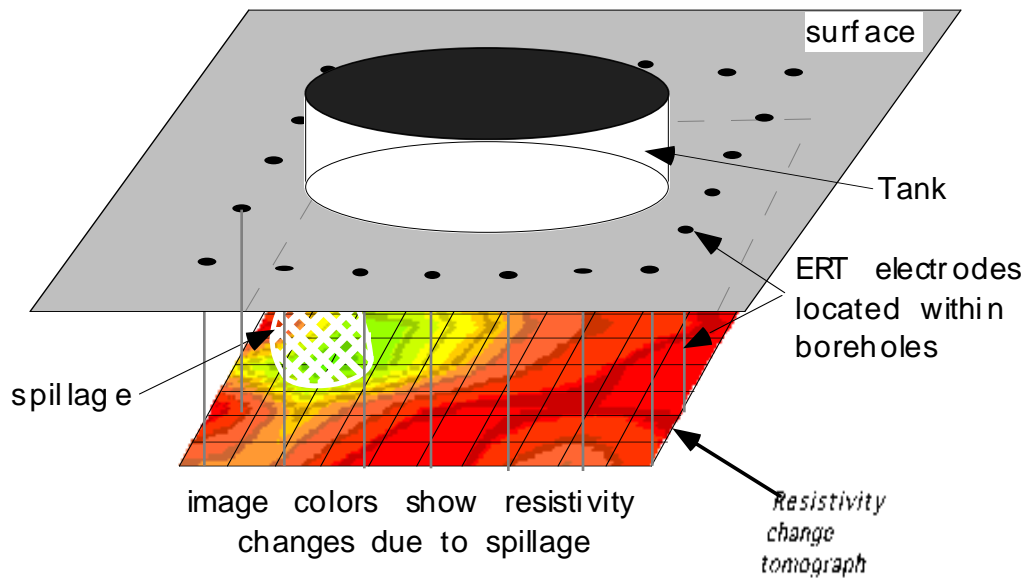
Figure 1. Schematic of the approach proposed for leak detection. The leak causes changes in the soil's electrical resistivity which are mapped using electrical resistance tomography.
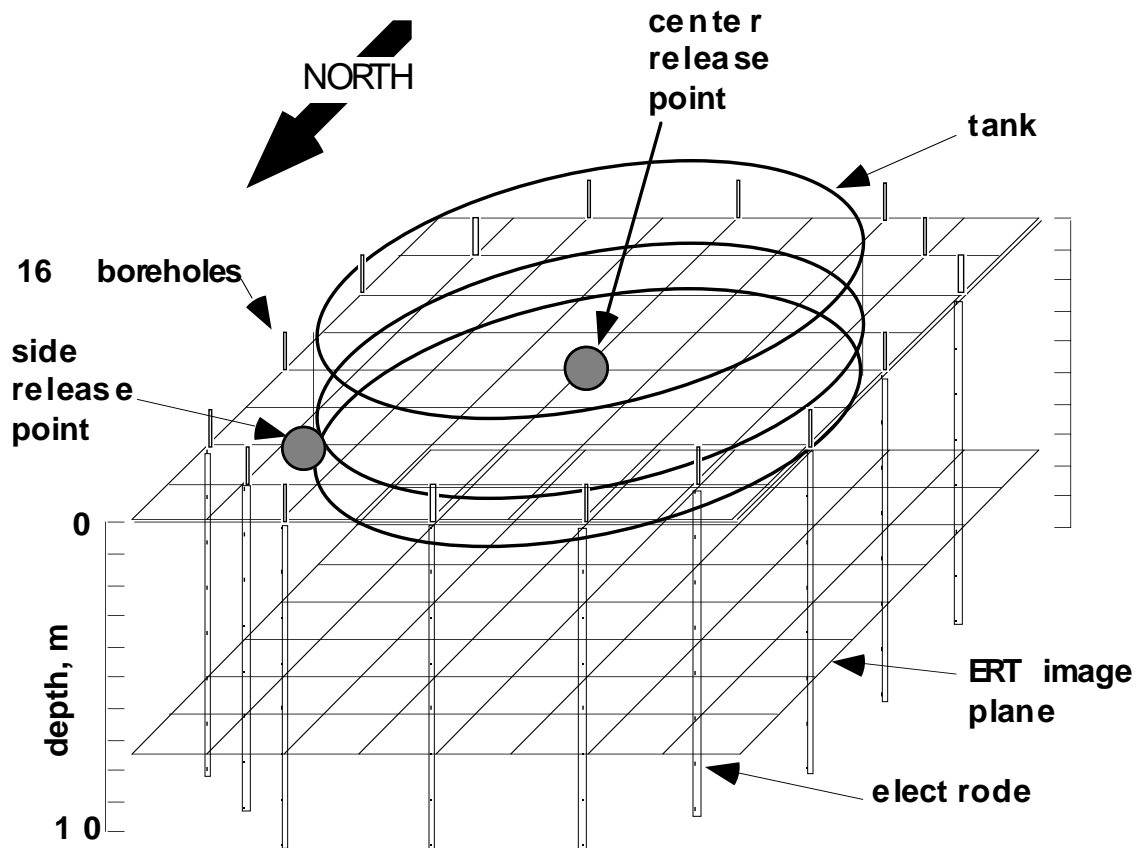
Figure 2. Schematic of experimental set up for leak detection. A 15 m diameter steel tank, the lower 2 meters of which is buried, contains several built-in spill point; results obtained using two of

these spill points will be discussed. Sixteen boreholes, with eight electrodes in each, surround the tank.
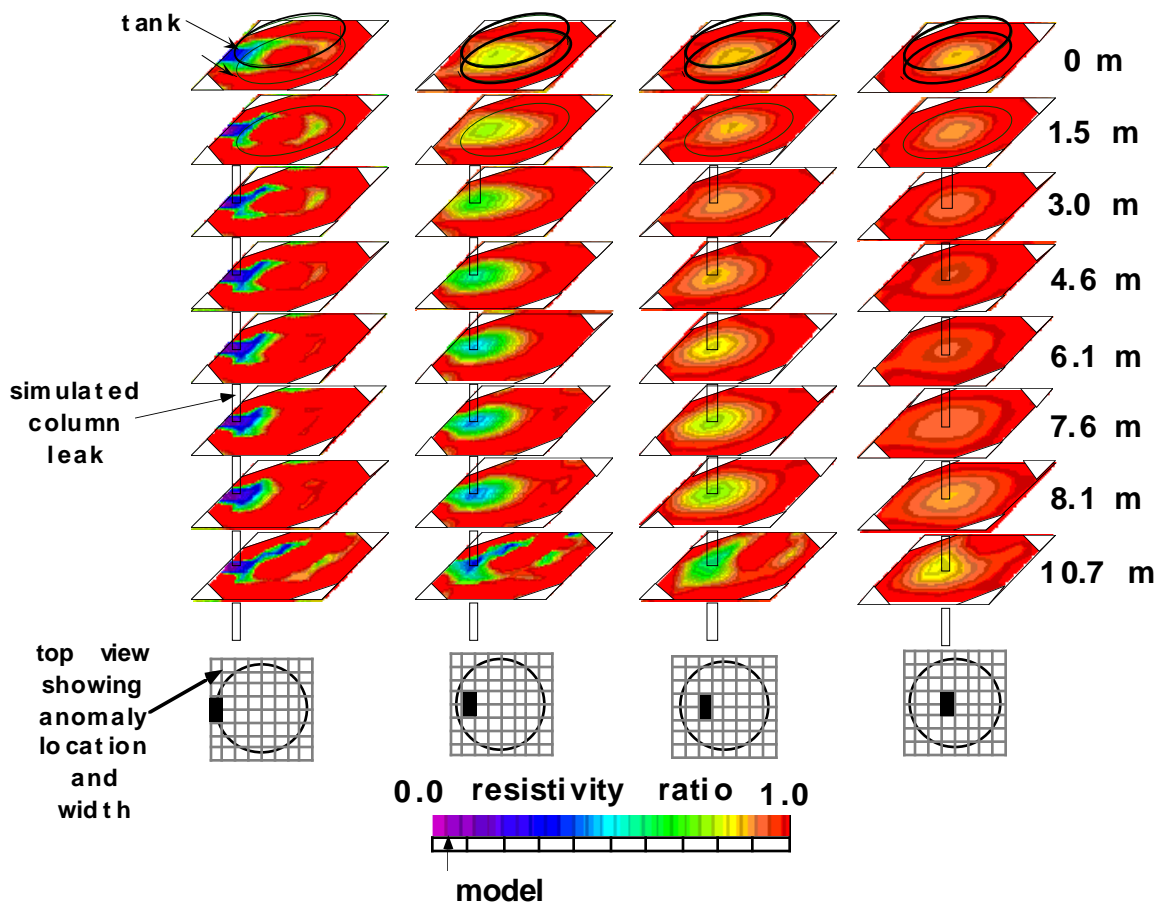
Figure 3. The results of numerical simulations are shown to illustrate how the reconstructed magnitude of a vertical column leak changes as a function of lateral position. Maximum magnitude (close to the model value) is reconstructed for changes occurring by the tanks edge while substantially reduced changes are reconstructed by the tank's center.

**model
(tank present
or absent)**

**tank
absent**

**tank
present**

0.0   resistivity ratio   1.0

↑
model
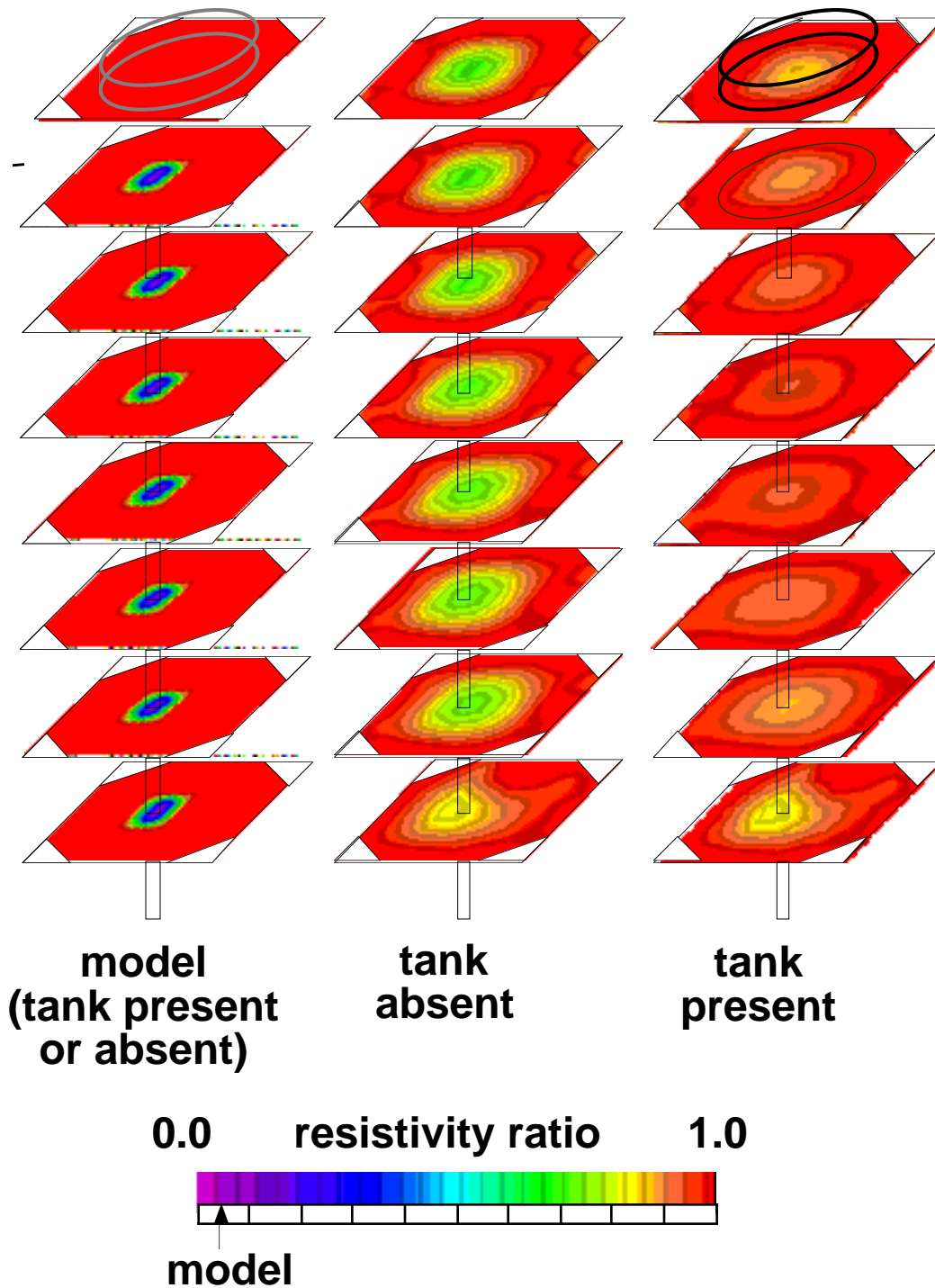
Figure 4. The results of numerical simulations are shown to illustrate the effects of a metal tank on the magnitude of a vertical column leak near the tank's center. Higher magnitudes are reconstructed when the tank is absent than when the tank is present.
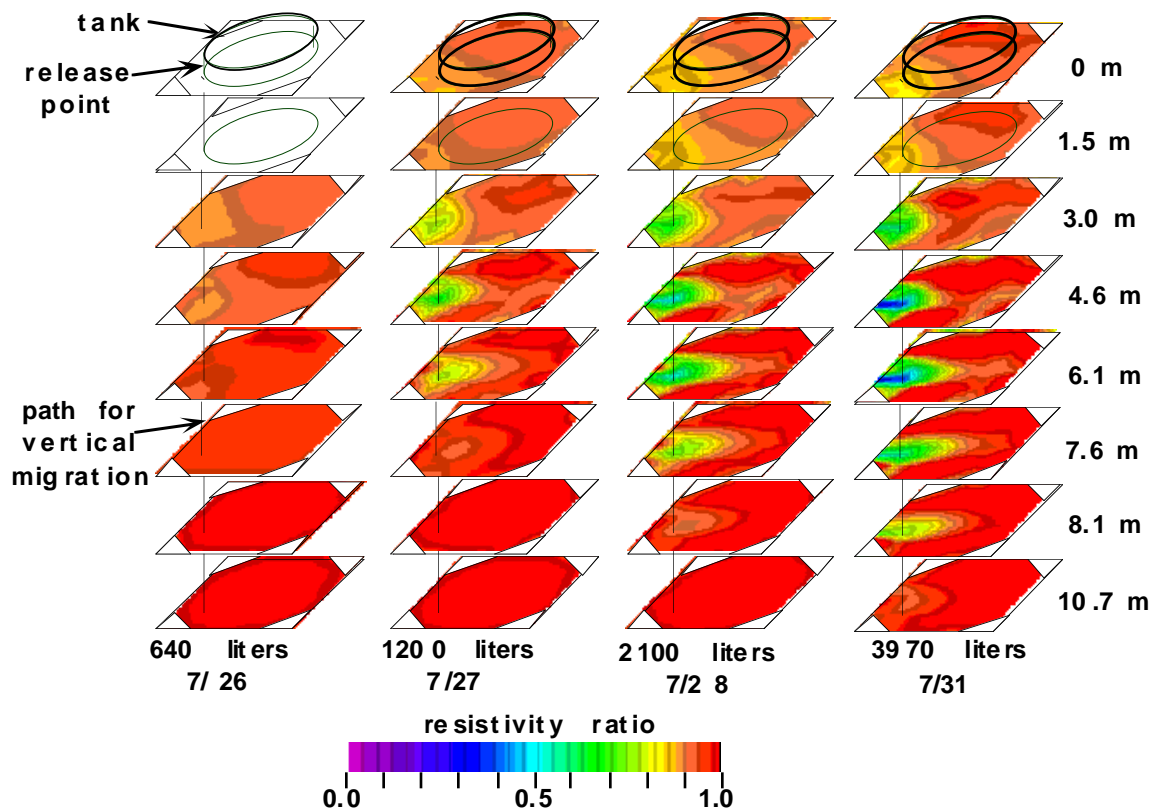
Figure 5 shows a series of two-dimensional ERT tomographs which show how the electrical resistivity of the soil decreased during the side release experiment. These tomographs were calculated with the algorithm described in section 1.3.1. Red colors indicate which portions of the images remain unchanged. Colors to the left of red indicate which portions of the image sho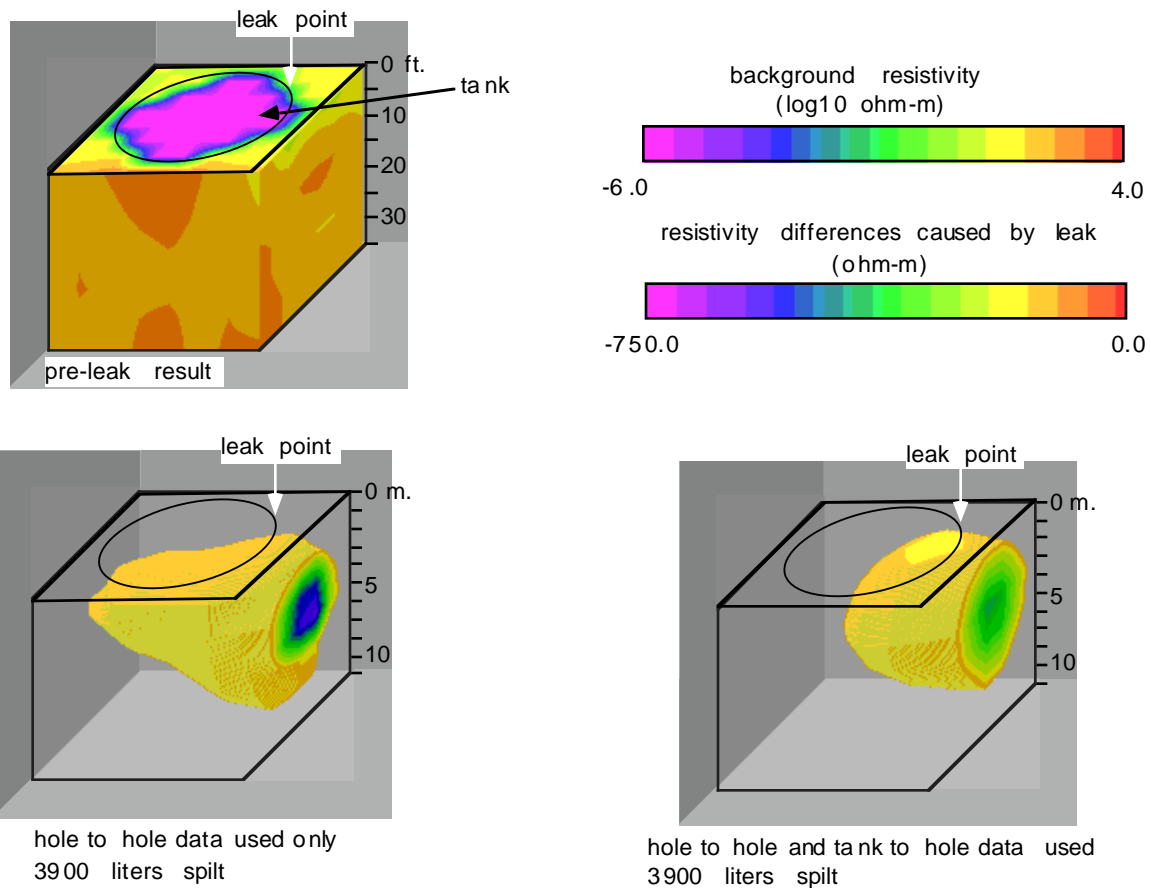w electrical resistivity decreases associated with the leak. A vertical black line shows the trajectory the brine would follow if it moved straight down.
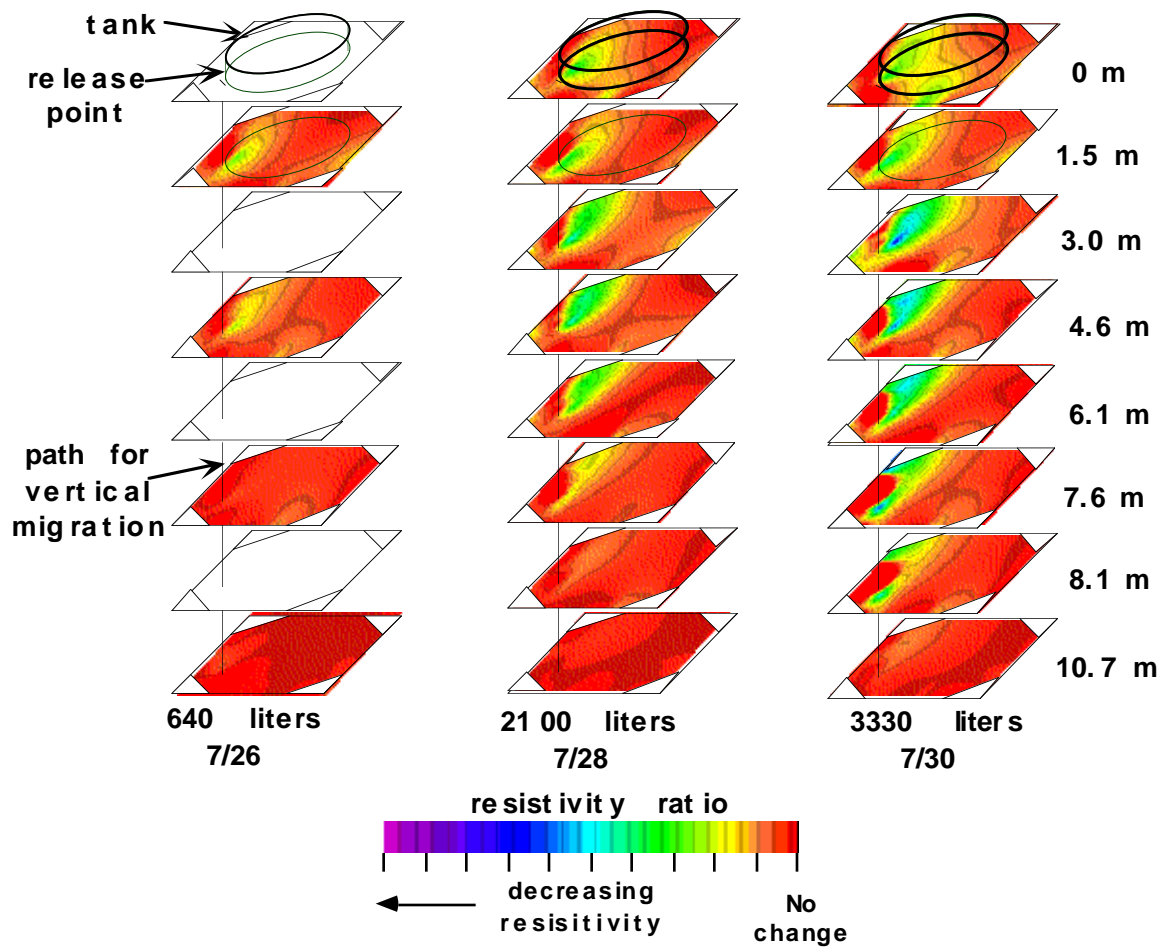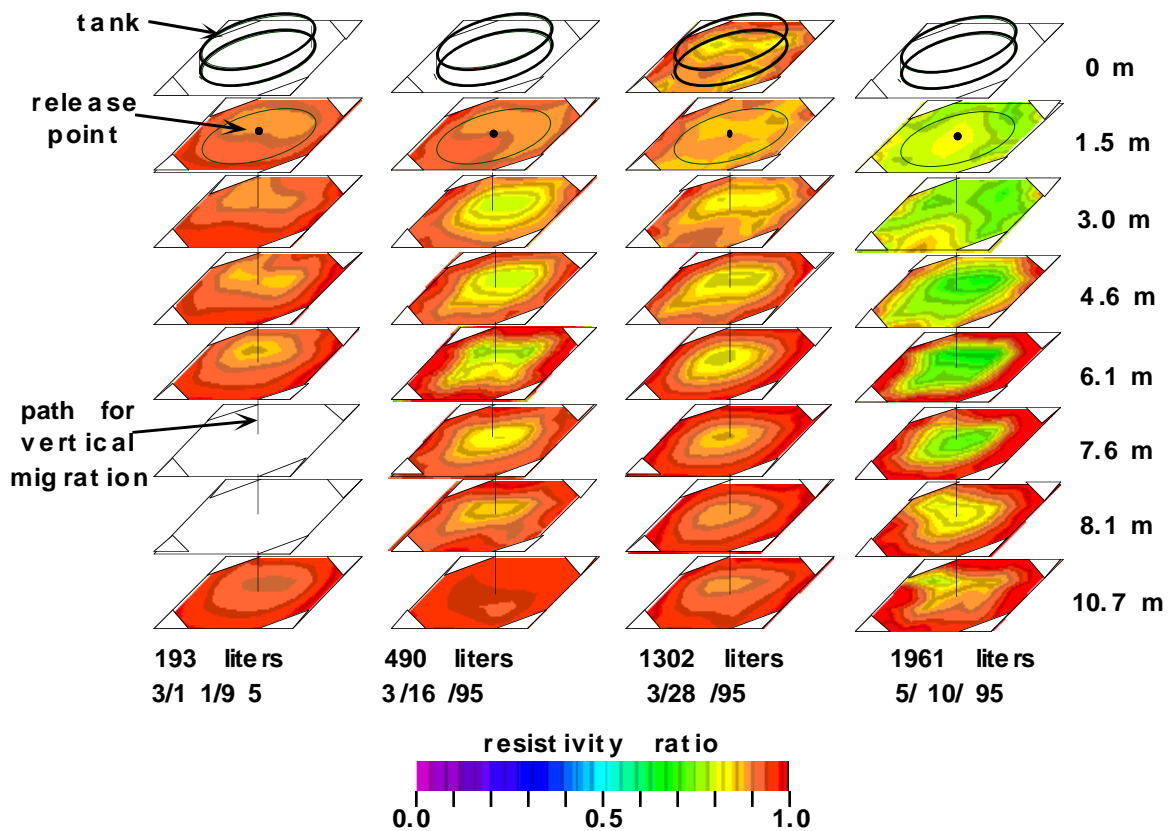
Figure 6 shows a series of two-dimensional ERT tomographs which show how the electrical resistivity of the soil decreased during the side release experiment. These tomographs were calculated with the algorithm described in section 1.3.2. Note that the changes shown in this case are qualitative. These results are similar to those in Figure 5.
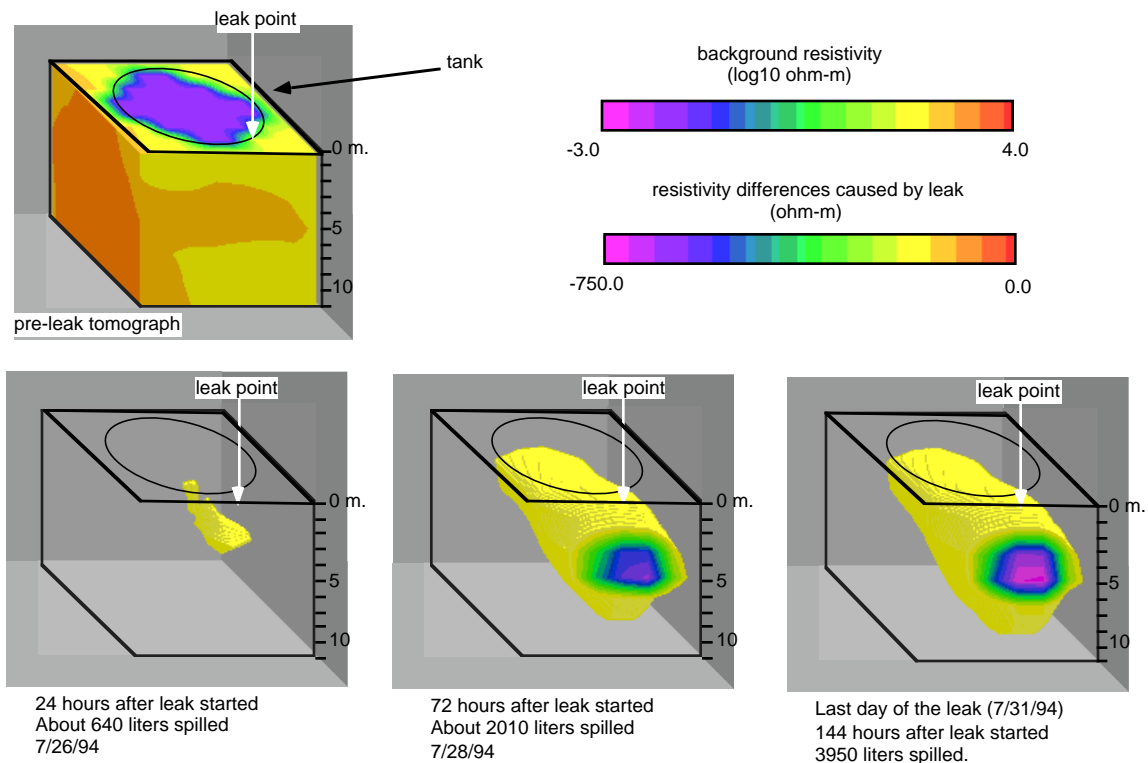
Figure 7 shows three-dimensional resistivity changes caused by the side release experiment. The bottom three images are transparent where the resistivity differences observed were less than 150 ohm-m. Colors to the left of red indicate which portions of the image show electrical conductivity increases (resistivity decreases) associated with the leak.

leak point

tank

0 ft.

10

20

30

pre-leak result

background resistivity
(log10 ohm-m)

-6.0   4.0

resistivity differences caused by leak
(ohm-m)

-750.0   0.0

leak point

0 m.

5

10

hole to hole data used only
3900 liters spilt

leak point

0 m.

5

10

hole to hole and tank to hole data used
3900 liters spilt

Figure 8 shows how the resistivity tomographs change when the tank is used as an electrode in combination with electrodes in the boreholes. The bottom two images show resistivity differences on the last day of the release; these images are transparent where the resistivity differences observed were less than 150 ohm-m. The data for the top left and bottom left images were collected using only the electrodes in the boreholes. The data for the right image was collected using the tank as an electrode as well as the borehole electrodes.

Figure 9 shows a series of two-dimensional ERT tomographs which show how the electrical resistivity of the soil decreased during the center release experiment. The 3/11/95 images at depths of 0, 4.6, 7.6 and 8.1 m are not shown because these data were not collected at this time. Red colors indicate which portions of the images remain unchanged. Colors to the left of red indicate which portions of the image show electrical conductivity increases associated with the leak. The range of values represented by the color used is identical used is identical to that used to depict the side release results in Figure 5. A vertical black line shows the trajectory the brine would follow if it moved straight down.

resistivity differences caused by noise
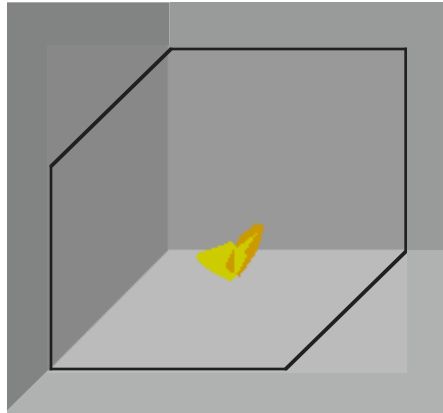
differences after approx. 1200 liters

NORTH

Leak point
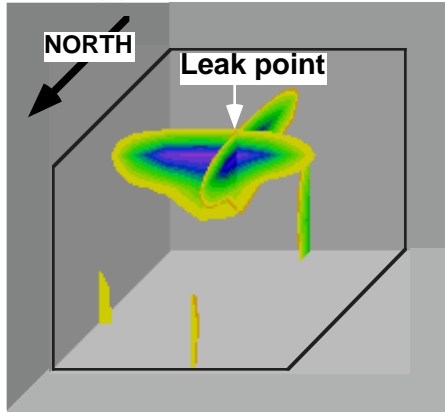
differences after approx. 1900 liters

metal casing analogue
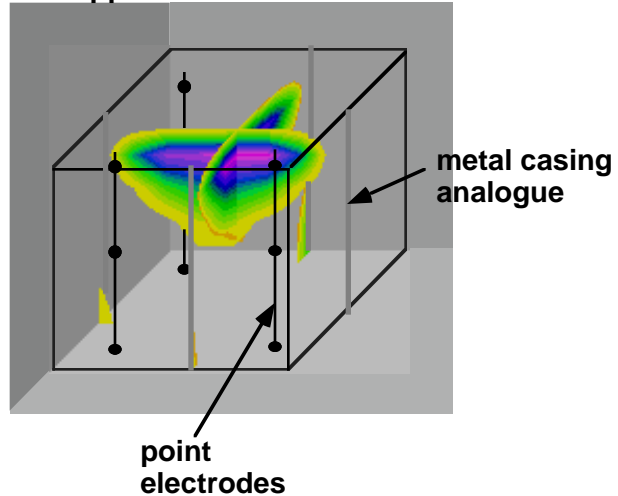
point electrodes

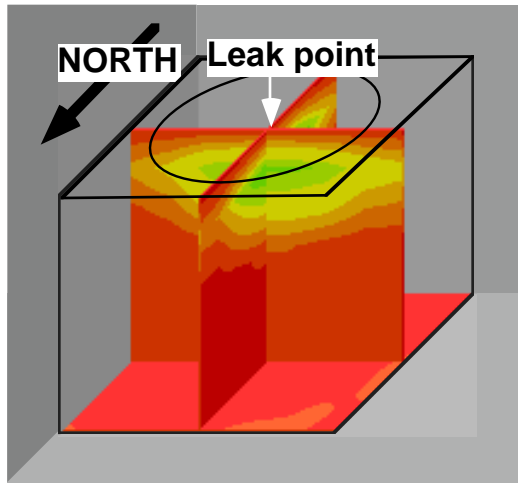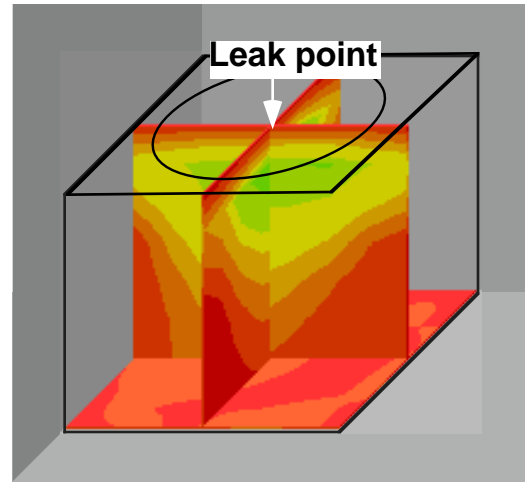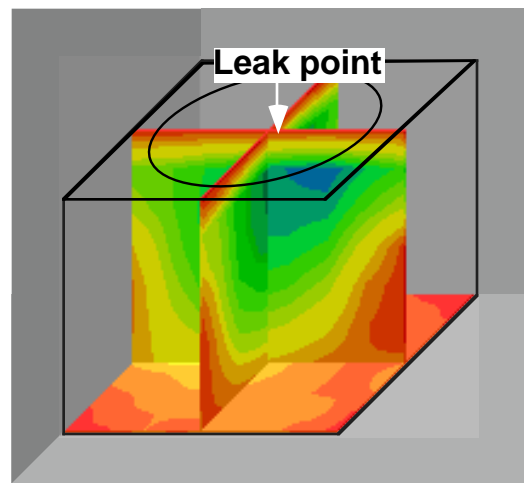**resistivity differences (ohm-m)**

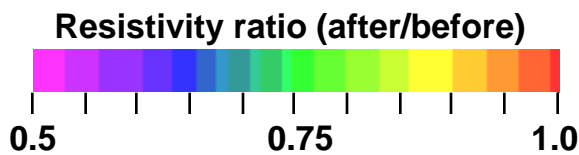-2000   -1000   0
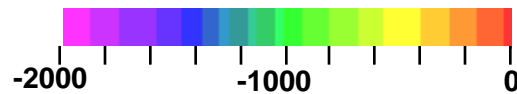
Figure 10 shows three-dimensional resistivity differences caused by the center release experiment. The resistivity surveys were conducted using four normal (point electrode) boreholes and four 'metal casing analogs'. The "metal casing analogs" were modeled as vertical columns of highly conducting elements which extended from the ground surface to 10.7 m depth.

NORTH **Leak point**

3/16/95 550 liters

Leak point

3/29/95 1200 liters

Resistivity ratio (after/before)

0.5   **0.75**   **1.0**

Leak point

5/10/95 1900 liters

Figure 11 shows three-dimensional resistivity ratios reconstructed for the center release experiment. The resistivity surveys were conducted using all 16 boreholes. The three dimensional resistivity ratios yield results comparable to resistivity differences but require only half the time for inversion.

16 boreholes   **8 boreholes**   **4 boreholes**

0 m

1.5 m

3.0 m

4.6 m
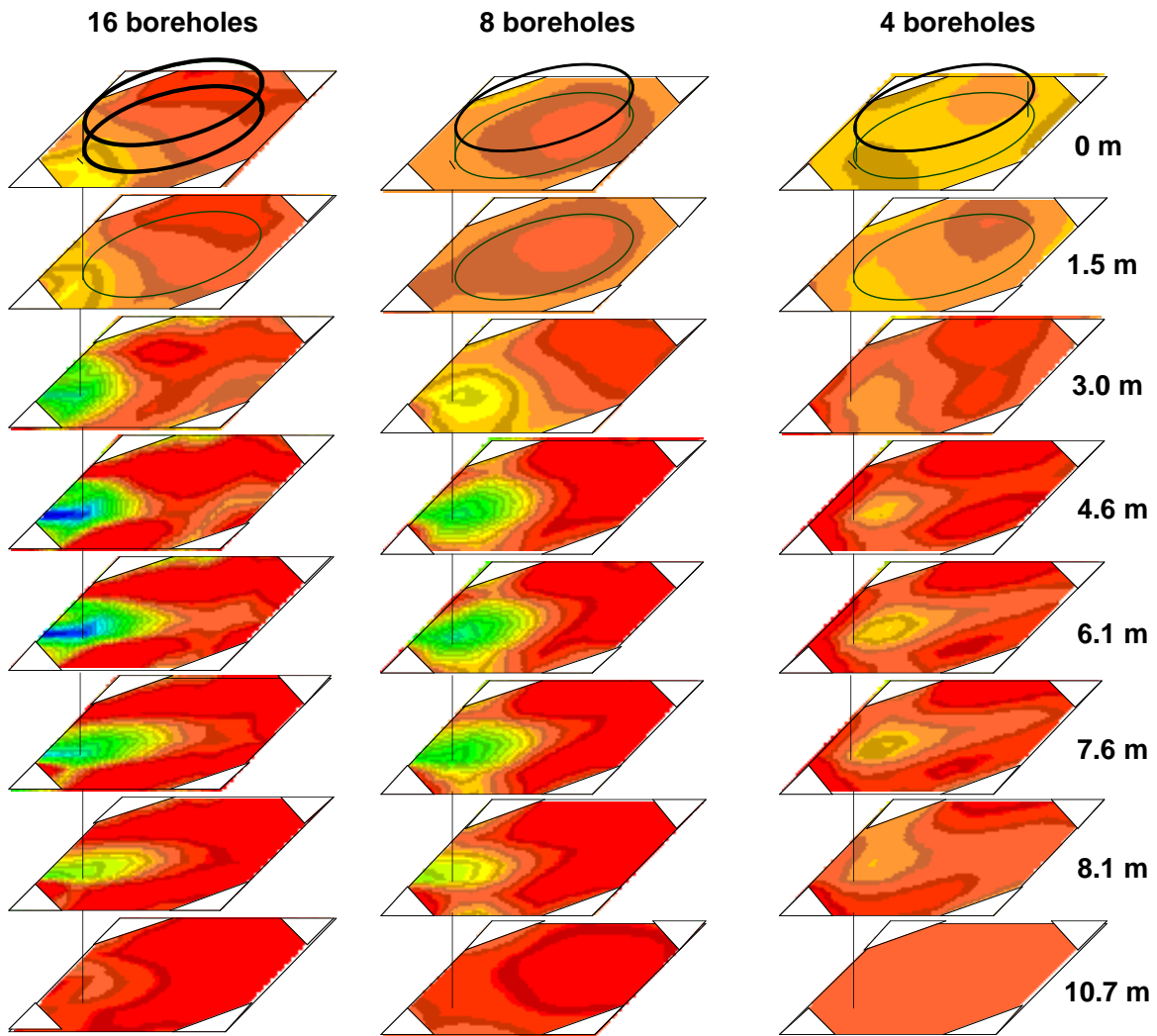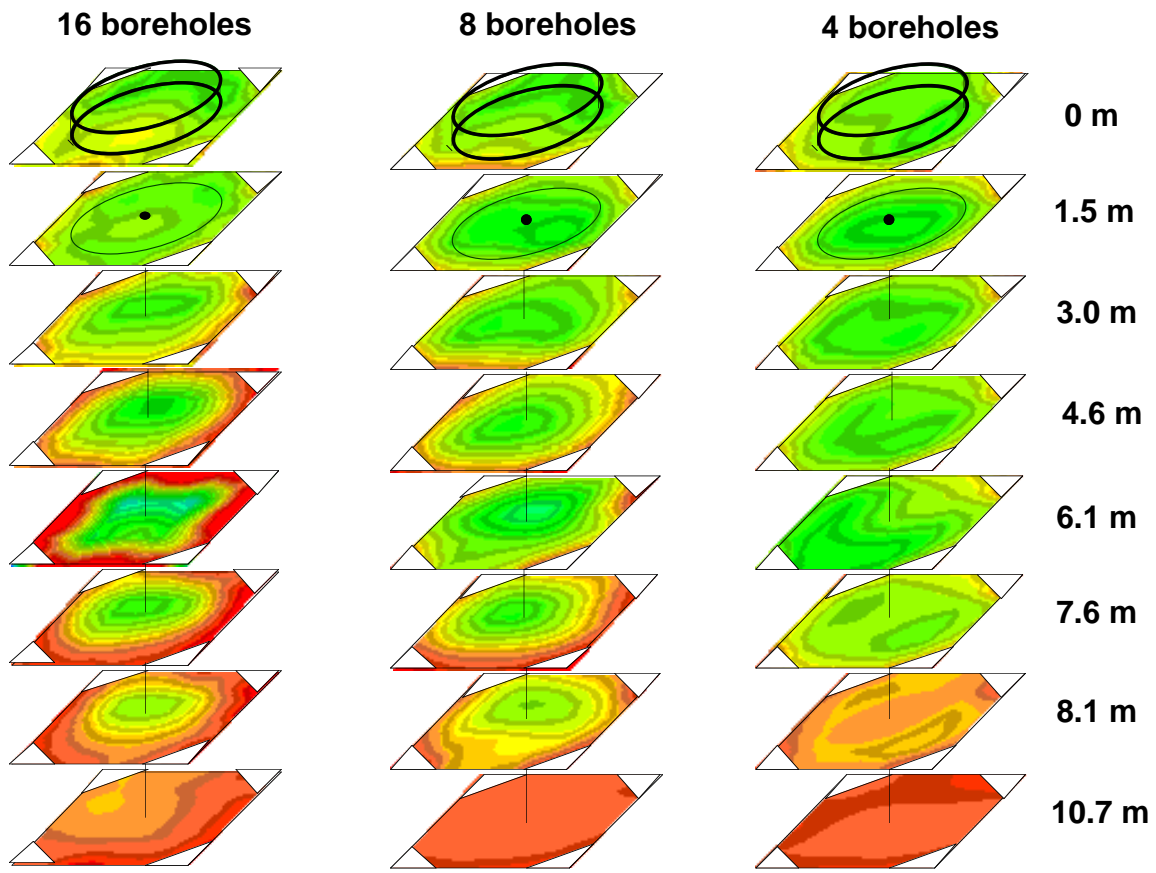
6.1 m

7.6 m

8.1 m

10.7 m

Figure 12 compares the July 31, 1994 results for the side release when data from all sixteen boreholes is used, with the results obtained with eight boreholes and with four boreholes. The color scale used is identical to the one used in Figure 5.

16 boreholes **8 boreholes** **4 boreholes**

0 m
1.5 m
3.0 m
4.6 m
6.1 m
7.6 m
8.1 m
10.7 m

data collected after approximately 1000 liters were released

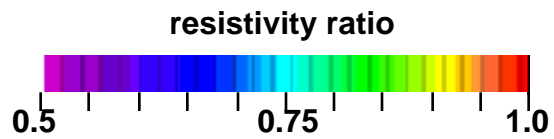**resistivity ratio**

0.5   **0.75**   **1.0**

Figure 13 compares the March 19-20, 1995 results for the center release when data from all sixteen boreholes is used, with the results obtained with eight boreholes and with four boreholes.